Nanoscale

RSC Publishing

PAPER

View Article Online
View Journal | View Issue

Cite this: *Nanoscale*, 2013, **5**, 8555

Nanocrystal shape and nanojunction effects on electron transport in nanocrystal-assembled bulks†

Shao-Chien Chiu,[a] Jia-Sin Jhang,[a] Yen-Fu Lin,[a] Shih-Ying Hsu,[a] Jiye Fang[b] and Wen-Bin Jian*[a]

Received 22nd March 2013
Accepted 25th June 2013

DOI: 10.1039/c3nr01418e

www.rsc.org/nanoscale

Bulk nanostructured materials are made from the assembly of octahedral PbSe nanocrystals. After thermal annealing, the artificial bulk demonstrates a large difference in behavior depending on the temperature, and a large variation of room-temperature resistivity of up to seven orders of magnitude. This variation originates from the high-indexed sharp edges of the octahedral nanocrystals. As the nanocrystals are arranged in the edge-to-edge configuration, which was observed in scanning electron microscopy images, the inter-nanocrystal capacitance is small due to the small parallel area between the nanocrystals. The small capacitance results in a high thermal fluctuation voltage and drives electron transport. The temperature-dependent resistivity and the electric field-dependent current are highly in agreement with the model of fluctuation-induced tunneling conduction. Thermal annealing reduces the inter-nanocrystal separation distance, creating a large variation in the electrical properties. Specifically, octahedral-shaped PbSe nanocrystals are employed in tailoring the electron transport in bulk nanostructured materials.

Introduction

Bulk nanostructured materials with microstructures of a characteristic length on the nanometer scale have been synthesized by either thermal equilibrium or non-equilibrium methods by controlling the sizes, dimensionality, atomic structures and alloying components.[1] The important process of non-equilibrium nanostructuring implements severe plastic deformation for the introduction of a high density of dislocations to enhance the physical properties of both the mechanical strength and ductility for metals.[2] The idea of tuning the physical properties in nanostructured materials has been reported elsewhere. For example, nanoparticle self-assembly,[3] a thermal-equilibrium nanostructuring method, made a bulk material showing distinct electrical and optical properties, thereby paving the way to tailoring new artificial electronic materials. The uniform size distribution and spherical shape of the artificial atoms facilitates their bulk assembly and the systematic modulation of electrical coupling between the semiconductor nanocrystals (NCs) or metal nanoparticles.[3,4] For future applications in electronics, methods of tuning the electrical properties of the artificial NC-assembled bulks is always a fascinating topic.

The electrical properties of NC-assembled bulks are strongly dependent on the interparticle separation distance. For a long interparticle distance, a threshold voltage and power law behavior between the current and voltage are commonly observed.[5] This collective Coulomb blockade effect has been observed at temperatures below the charging energy of the NC, and was well described by the Middleton–Wingreen model.[6] In particular, the interparticle distance can be adjusted by a molecular linker. For example, gold NC-assembled three-dimensional ordered arrays in silica exhibited the collective Coulomb blockade effect[7] while, in contrast, gold NC arrays linked by shorter molecular linkers revealed thermally activated transport. With a gradual increase of the length of the molecular linker, the room-temperature (RT) resistivity of the gold NC-assembled bulk increased by up to six orders of magnitude.[8] For an ultra-short alkanedithiol molecular linker five carbon atoms long, the gold NC-assembled bulk revealed metallic behavior, namely a monotonic increase in resistivity with rising temperature.[9] Another transition from insulating to metallic conductivity was observed when the NCs were melted and connected together to form a granular bulk.[10]

Other electron transport mechanisms in the NC-assembled bulk are discussed for the case of medium interparticle distances where thermally activated transport is commonly observed at high temperature. The phase of the electron is conserved with a decrease in temperature, thus variable-range-hopping (VRH) transport emerges. In addition, the Coulomb

[a]*Department of Electrophysics, National Chiao Tung University, Hsinchu 30010, Taiwan, ROC. E-mail: wbjian@mail.nctu.edu.tw*

[b]*Department of Chemistry, State University of New York at Binghamton, Binghamton, New York 13902-6000, USA*

† Electronic supplementary information (ESI) available: additional details about (I) experiments and device information, (II) particle size distribution, (III) capping agents, (IV) inter-particle capacitances, (V) devices of metallic features, (VI) fitting to Fig. 3(a), (VII) fitting parameters and (VIII) statistics on the arrangements between neighboring nanocrystals. See DOI: 10.1039/c3nr01418e

energy of the NCs takes effect for ultra-small NCs. Heath's group reported[11] the Efros–Shklovskii VRH[12] at high temperature and the collective Coulomb blockade effect at low temperature. They discovered the crossover from two- to one-dimensional electron transport for both of the transport models. Moreover, Guyot-Sionnest's group depicted[13] a crossover transition between Mott[14] and Efros–Shklovskii[12] VRH as a function of temperature and the density of states. On the other hand, electron transport in random materials[15] or nanoporous thin films[16] was commonly attributed to Sheng's model of fluctuation-induced tunneling conduction[17,18] (FITC). Many transport mechanisms have been proposed for electron transport in NC-assembled bulks but the details of how electrons tunnel between NCs have not been investigated. To disregard the Coulomb blockade effect, we employed large NCs to assemble a bulk material. In addition, we used octahedral rather than spherical NCs to explore the shape effect.

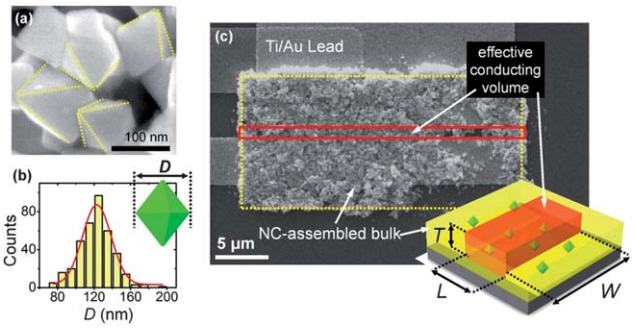

Fig. 1 (a) SEM image of the octahedral PbSe NCs. The yellow dotted lines show the outlines of individual NCs. (b) Statistical distribution of the NC size (D), marked in the inset, with a Gaussian function fitting. (c) SEM image of a typical NC-assembled bulk device. The yellow dotted line and the red solid line indicate the frame of the NC-deposited area and the effective conducting volume, respectively. The inset presents a scheme of the device corresponding to the SEM image. The effective conducting volume of the NC-assembled bulk is of L in length, W in width and T in thickness.

Experimental

Octahedral PbSe NCs capped with oleic acid and trioctylphosphine were size-selected from the products prepared according to the method of ref. 19, and it was determined that the component of Mn in these PbSe NCs is insignificant and can be neglected. The as-synthesized NCs were stored in hexane. Before assembly, a trench of 25 μm in length, 1 μm in width and 20 nm in depth was formed between two Pt electrodes which were patterned by electron-beam lithography in connection with photo-lithography pre-patterned Ti/Au electrodes on a silicon wafer. The prepared substrate was spin-coated with 400 nm thick PMMA and patterned by electron-beam lithography, again, to develop a PMMA window of 25 × 12.5 μm^2 directly on the top of the trench. The stored PbSe NC suspension was drop-cast on the PMMA-protected substrate for NC deposition onto the window-opened trench. After the substrate was dried in air, it was immersed in acetone for 1 h to remove the PMMA protecting layer. The substrate was dried by a flow of nitrogen gas, and a small piece of PbSe NC-assembled bulk was molded into the trench and onto the pair of Pt electrodes (Section I, ESI†). The as-deposited, NC-assembled bulk exhibited a resistance higher than 10^{12} Ω at RT. To reduce the sample resistance, it was annealed at 225, 250 and 275 °C for 10–360 min under a high vacuum. Such a thermal treatment may remove some capping agents from the surface of the PbSe NCs. The morphology and dimensions of the NC-assembled bulk were measured using a scanning electron microscope (SEM, JEOL JSM-7000F) and the thickness of the NC-assembled bulks was determined to be about 1 μm using an atomic force microscope (Seiko Instruments Inc. SPA-300HV). Finally, the sample was loaded into a cryostat (Variable Temperature Insert Cryostat, CRYO Industries of America Inc.) for temperature-dependent electrical characterization.

Results and discussion

A PbSe nano-octahedron (SEM image in Fig. 1a) possesses twelve edges and six apexes. The average diameter (D) was statistically estimated to be 122 ± 18 nm from the SEM image (Section II, ESI†), and is presented in Fig. 1b. Such large NCs were used to make the nanostructured bulk. Generally, two types of capacitance, self- and inter-NC capacitances, are considered for electron transport in the NC-assembled bulk. The self-capacitances of the NCs induce a Coulomb charging energy to block the tunneling of other electrons. Taking PbSe NCs as simple spheres without the consideration of any sharp apexes and edges, the self-capacitance induced charging energy (E_C) is only ~0.19 meV, according to the expression of $E_C = e^2w/(4\pi\varepsilon\varepsilon_0 D(D/2 + w))$,[20] where $w \cong 2$ nm is the separation distance between the NCs (Section III, ESI†) and $\varepsilon \cong 2$ is the dielectric constant of the capping agents. Because of the negligible Coulomb energy, we can exclude the transport mechanisms of the Middleton–Wingreen model[6] and ES hopping conduction[12] in this system. The NC-assembled nanostructured bulk was imaged as shown in Fig. 1c, with a corresponding scheme displayed in the inset. The boundary of the solid lines in red indicates the top view of the effective conducting volume, which has dimensions of $L \cong 1$ μm, $T \cong 1$ μm and $W \cong 25$ μm (Section I, ESI†). In addition to the charging energy of the PbSe NCs, the effect of the thermal fluctuation voltage due to the inter-NC capacitance needs to be considered (Section IV, ESI†).

The PbSe NC-assembled bulk materials were annealed at three different temperatures and their topographies were scrutinized using an SEM (see Fig. 2a–c). The post-annealing at either 225 or 250 °C does not generate any major morphological variation while the annealing at 275 °C drives a meltdown process which causes the interconnection of the PbSe NCs and formation of granular thin film. The RT resistivity variation of the NC-assembled bulks under various annealing temperatures and times are presented in Fig. 2d. It can be seen that the RT resistivity of the NC-assembled bulk was much higher than 10^9 Ω cm before any thermal treatment. After annealing at a temperature above 225 °C, the RT resistivity drops by three orders of magnitude to ~10^6 Ω cm and further falls to lower

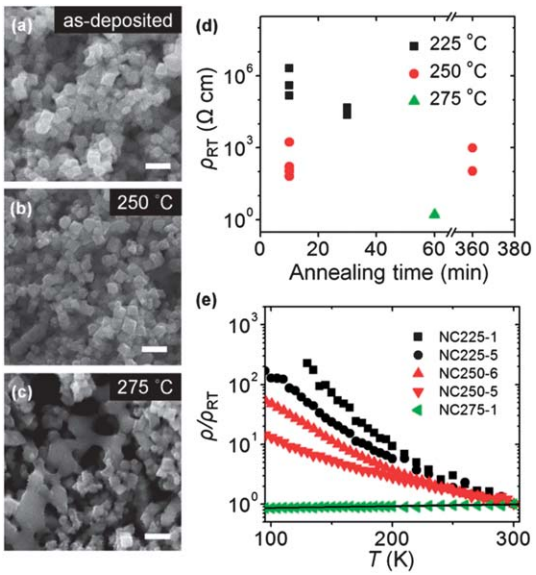

Fig. 2 SEM images of (a) the as-deposited PbSe NC-assembled bulk, (b) the nanostructured bulk annealed at 250 °C for 6 h and (c) at 275 °C for 1 h. The scale bars in the three images represent 200 nm in length. (d) RT resistivity of the nanostructured bulk as a function of the annealing time at three different annealing temperatures. (e) Temperature behavior of five representative NC-assembled bulks annealed at 225, 250, or 275 °C. The resistivity is normalized by dividing by the RT resistivity. The black line is the linear least square fitting to the data of the nanostructured bulk annealed at 275 °C.

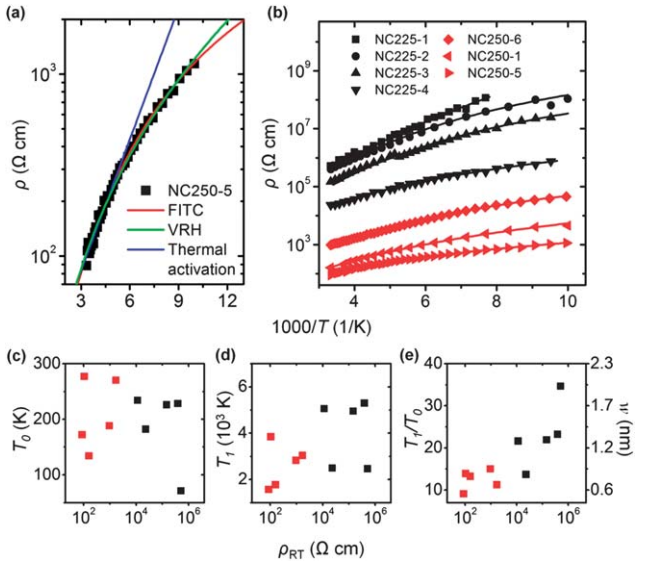

Fig. 3 (a) Typical temperature-dependent resistivity behavior with fittings to the FITC, the Mott 3D VRH, and the thermal activation models. (b) Resistivity in the logarithm scale, as a function of the inverse temperature, of the PbSe NC-assembled bulks annealed at 225 (black) and 250 °C (red). The solid lines present the best fit to the data. Fitting parameters (c) T_0 and (d) T_1 are displayed as a function of the RT resistivity of the nanostructured bulk. (e) The ratio of T_1/T_0 and the estimated inter-particle distance w as a function of the RT resistivity.

than 10^5 Ω cm for a longer period of annealing. With an increase of the annealing temperature to 250 °C, the RT resistivity of the NC-assembled bulk decreases to about 10^2 Ω cm (Section I, ESI†). As shown in Fig. 2b, the morphology of the NC-assembled bulk does not change, whereas its RT resistivity changes by up to seven orders of magnitude, manifesting a large variation in electron transport. Raising the annealing temperature to 275 °C triggers a meltdown process and the resistivity of the NC-assembled bulk descends further to about 1 Ω cm. The insulator-to-metal transition induced by melting is similar to that reported previously.[10]

In addition to the RT resistivities, the temperature behavior of several typical NC-assembled bulks is presented in Fig. 2e. With a decrease in the observation temperature to 100 K, the resistivity increases by two or three orders of magnitude. Additionally, the $\rho_{100\ K}/\rho_{RT}$ ratio of the NC225-1 (high RT resistivity) device is about two orders of magnitude larger than that of the NC250-5 (low RT resistivity) device, indicating a difference of nine orders of magnitude for the resistivity at 100 K. The temperature behavior demonstrates non-metallic electrical properties for the NC-assembled bulk annealed at 225 or at 250 °C and metallic behavior for the bulk material annealed at 275 °C. The metallic feature of the RT resistivity and the temperature behavior of the NC275-1 device are in line with the properties of single-crystalline PbSe films reported previously (Section V, ESI†).[21] On the other hand, the non-metallic or semiconducting temperature behavior needs further investigation to clarify the physical mechanism which manipulates such a large conductivity variation.

Fig. 3a presents the resistivity as a function of the inverse temperature, and it best fits to three models: the FITC, the Mott three-dimensional (3D) VRH, and the thermal activation models. Since the data do not show linear behavior under the log $\rho - 1/T$ expression, we may eliminate the possibility of electron transport due to thermal activation. Likewise, neither shall we consider the transport mechanism of percolation because the thermal annealing does not drive reassembly of the NCs. In addition, the percolation model[22,23] predicts that the resistance has an exponential temperature dependence with $T^{-1/2}$, and that the current has a linear voltage dependence. This predicted behavior is inconsistent with our data. Moreover, the data fitting to the FITC model gives the smallest standard deviation in comparison with fittings to other models (Section VI, ESI†). The tunneling segment of nanoconstriction is less than 2 nm, which fulfils the condition of being less than half of the electron's Fermi wavelength in the PbSe NCs[18] and encourages the fitting to the FITC model. The temperature-dependent resistivities with fitting to the FITC model for all of the semiconducting devices are displayed in Fig. 3b. The FITC model predicts temperature behavior following the equation of $\rho(T) = \rho_0 \exp(T_1/(T + T_0))$,[17] where ρ_0 is a constant, and T_1 and T_0 are two parameters. The FITC model describes a tunneling current elevated by the thermal fluctuation voltage through a junction between two metal islands. If the junction has an area A, a barrier height V_0 and a width w, the two parameters T_1 and T_0 are expressed as $(8\varepsilon\varepsilon_0/e^2k_B)(AV_0^2/w)$ and $(16\varepsilon\varepsilon_0\hbar/\pi e^2k_B(2m)^{1/2})(AV_0^{3/2}/w^2)$, respectively, where m is the electron mass. The two parameters extracted from the fittings to the data in Fig. 3b are presented in Fig. 3c and d (Section VII, ESI†). It is noted that the two parameters do not expose any tendencies with respect to the device RT resistivity (ρ_{RT}) because

of the variation of the junction areas. Nevertheless, the ratio of T_1/T_0 shown in Fig. 3e reveals a strong dependence on the device RT resistivity and, by taking the junction barrier V_0 as 4.56 eV,[24] the junction widths are estimated. Fig. 3e shows that the decrease of the junction width, as well as the separation distance between the PbSe NCs, causes a decrease in the RT resistivity of the NC-assembled bulks.

To confirm the agreement between the real transport mechanism in the NC-assembled bulk and the FITC model, we carried out *I–V* measurements under high electric fields and analyzed the data using the FITC and the Mott 3D VRH models (Fig. 4a and b). The FITC model predicts high-field *I–V* according to the equation $I \cong I_0 \exp\{-a(T)[(V/V') - 1]^2\}$,[17] where I_0 is a weak temperature- and electric field-dependent parameter, $a(T)$ is a temperature-dependent parameter and V' is a parameter in relation to the junction parameters of the width w and the barrier V_0 (Section VII, ESI†). The *I–V* data of the typical NC225-3 device in Fig. 4a firmly follow the FITC model and, more precisely, the evaluated $a(T)$ parameter at various temperatures (closed squares in the inset of Fig. 4a) obeys the equation $a(T) = T_1/(T + T_0)$, where the T_0 and T_1 parameters are estimated from the temperature behavior shown in Fig. 3b. The results strongly suggest that the FITC model correctly describes the electron transport in the PbSe NC-assembled bulk. On the other hand, the Mott 3D VRH model offers the electric field dependence according to the form of $\log \rho \sim E^{-1/4}$.[25] Fig. 4b clearly shows the inconsistency between the experimental data and the Mott 3D VRH model, thus this model is excluded from the contributions to electron transport in the PbSe NC-assembled bulk. Now we turn to identify the junction which is described by the FITC model. Fig. 4c presents an SEM image of the PbSe NC-assembled bulk. There are two types of arrangements between neighboring PbSe NCs. One is face-to-face and the other is edge-to-edge configuration. The edge-to-edge configuration of

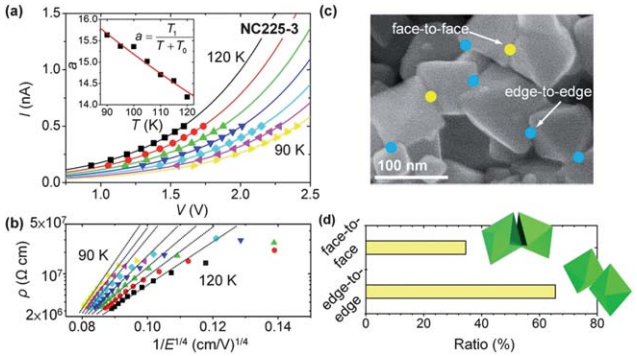

Fig. 4 (a) High-field *I–V* curves at 120 K (squares), 115 K (circles), 110 K (upper triangles), 105 K (lower triangles), 100 K (diamonds), 95 K (left triangles) and 90 K (right triangles). The solid lines are curve fittings according to the FITC model. The inset shows the parameters estimated from the fittings. The solid line in the inset indicates the temperature dependence of $a(T) = T_1/(T + T_0)$, where $T_0 = 226$ K and $T_1 = 4950$ K, extracted from NC225-3 in Fig. 3b. (b) Electric field dependence of the resistivity ($\log \rho - E^{-1/4}$) of the NC225-3 device at various temperatures corresponding to the data in (a). The solid lines are curve fittings according to the Mott 3D VRH model. (c) SEM image revealing the face-to-face and edge-to-edge configurations of the PbSe NCs. (d) Ratio of the two configurations calculated from the SEM image.

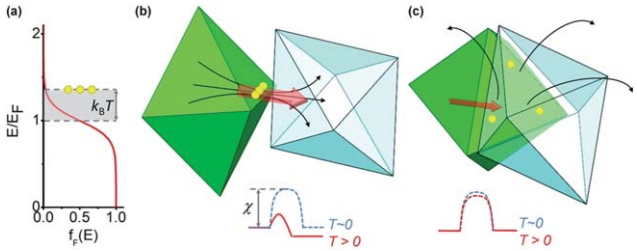

Fig. 5 (a) Scheme showing the Fermi distribution of electrons in the PbSe NCs and the occasionally excited electrons by thermal fluctuation. (b) Scheme showing thermally excited electrons arranged between NCs in the edge-to-edge configuration. Electrons distributed on an ultra-small junction area cause a high electric field which drives them across the junction. Alternatively, the high electric field lowers the junction potential barrier. (c) Scheme showing thermally excited electrons arranged between NCs in the face-to-face configuration. Electrons distributed on a large junction area generate a low electric field across the junction.

neighboring NCs was more commonly observed, as shown in the SEM image, than the face-to-face configuration. Their statistical data are presented in Fig. 4d (Section VIII, ESI†). The FITC model based on the two configurations needs to be explained further.

The FITC model describes occasionally excited electrons on one of the two neighboring NCs due to thermal energy (Fig. 5a). The excited electrons build up a thermal fluctuation voltage V_T between the two neighboring NCs, so as to drive electrons to tunnel through the neighboring NCs. The thermal fluctuation voltage is directly dependent on the inter-NC capacitance C, following the form $V_T = (k_B T/C)^{1/2}$. When the neighboring NCs are arranged in the edge-to-edge configuration shown in Fig. 5b, the ultra-small surface offers a tiny inter-NC capacitance of $\sim 10^{-20}$ F which generates a high thermal fluctuation voltage of $\sim$0.64 V (Section IV, ESI†). The emergence of the thermal fluctuation voltage can be taken as the lowering of the junction barrier between the two neighboring PbSe NCs. The effect is similar to the point discharge phenomenon. In contrast, the inter-NC capacitance of the neighboring NCs in the face-to-face configuration (Fig. 5c) does not give a high enough thermal fluctuation voltage to drive electrons to tunnel through the neighboring NCs. Consequently, the two thirds of the PbSe NCs arranged in the edge-to-edge configuration form highly conducting channels, which dominate electron transport in the NC-assembled bulk. The annealing of the NC-assembled bulk causes a decrease of the inter-NC separation distance and, simultaneously, a decrease of the bulk resistivity, which agrees well with the prediction of the FITC model. The special transport mechanism does not exist in other systems assembled by spherical NCs.

Conclusion

In summary, octahedral PbSe NCs were assembled into a micrometer bulk material, sitting in a trench between two metal electrodes for electrical characterization. Through a simple thermal annealing treatment, the resistivity of the NC-assembled bulk varies by up to seven and nine orders of magnitude at RT and low temperature, respectively. In addition, the

temperature coefficient of resistivity differs largely, which can be identified from the ratio of the low-temperature resistivity to the RT resistivity. Both the temperature and electric field dependent behavior suggest that the FITC is the best model to describe electron transport in the PbSe NC-assembled bulk. The special shape of octahedra results in edge-to-edge configuration between neighboring NCs, thus giving electron transport behaviors in good agreement with the FITC model. Such an edge-to-edge configuration offers an ultra-small capacitance and, simultaneously, generates a high thermal fluctuation voltage, thereby resulting in highly conducting channels in the bulk. By subsequent thermal annealing, the inter-NC separation distance is reduced so as to modulate the electrical properties.

Acknowledgements

This work was supported by the Taiwan National Science Council under grant numbers NSC 98-2112-M-009-013-MY2 and NSC 98-2923-M-009-001-MY2, and by the MOE ATU Program. JF thanks NSF's support (DMR-0731382).

References

1 H. Gleiter, *Acta Mater.*, 2000, **48**, 1.
2 R. Valiev, *Nat. Mater.*, 2004, **3**, 511.
3 A. Zabet-Khosousi and A. A. Dhirani, *Chem. Rev.*, 2008, **108**, 4072.
4 Y. C. Ou, J. J. Wu, J. Fang and W. B. Jian, *J. Phys. Chem. C*, 2009, **113**, 7887.
5 C. T. Black, C. B. Murray, R. L. Sandstrom and S. Sun, *Science*, 2000, **290**, 1131.
6 A. A. Middleton and N. S. Wingreen, *Phys. Rev. Lett.*, 1993, **71**, 3198.
7 H. Fan, K. Yang, D. M. Boye, T. Sigmon, K. J. Malloy, H. Xu, G. P. López and C. J. Brinker, *Science*, 2004, **304**, 567.
8 W. P. Wuelfing, S. J. Green, J. J. Pietron, D. E. Cliffel and R. W. Murray, *J. Am. Chem. Soc.*, 2000, **122**, 11465.
9 A. Zabet-Khosousi, P. E. Trudeau, Y. Suganuma, A. A. Dhirani and B. Statt, *Phys. Rev. Lett.*, 2006, **96**, 156403.
10 P. Beecher, A. J. Quinn, E. V. Shevchenko, H. Weller and G. Redmond, *Nano Lett.*, 2004, **4**, 1289.
11 K. Xu, L. Qin and J. R. Heath, *Nat. Nanotechnol.*, 2009, **4**, 368.
12 A. L. Efros and B. I. Shklovskii, *J. Phys. C: Solid State Phys.*, 1975, **8**, L49.
13 H. Liu, A. Pourret and P. Guyot-Sionnest, *ACS Nano*, 2010, **4**, 5211.
14 N. F. Mott, in *Metal–Insulator Transitions*, Taylor & Francis, London, 1990.
15 A. B. K. Chen, S. G. Kim, Y. Wang, W. S. Tung and I. W. Chen, *Nat. Nanotechnol.*, 2011, **6**, 237.
16 S. J. Konezny, C. Richter, R. C. Snoeberger, A. R. Parent, G. W. Brudvig, C. A. Schmuttenmaer and V. S. Batista, *J. Phys. Chem. Lett.*, 2011, **2**, 1931.
17 P. Sheng, E. K. Sichel and J. I. Gittleman, *Phys. Rev. Lett.*, 1978, **40**, 1197.
18 H. Xie and P. Sheng, *Phys. Rev. B: Condens. Matter Mater. Phys.*, 2009, **79**, 165419.
19 W. Lu, P. Gao, W. B. Jian, Z. L. Wang and J. Fang, *J. Am. Chem. Soc.*, 2004, **126**, 14816.
20 B. Abeles, P. Sheng, M. D. Coutts and Y. Arie, *Adv. Phys.*, 1975, **24**, 407.
21 J. N. Zemel, J. D. Jensen and R. B. Schoolar, *Phys. Rev.*, 1965, **140**, A330.
22 E. Šimánek, *Solid State Commun.*, 1981, **40**, 1021.
23 K.-H. Müller, J. Herrmann, B. Raguse, G. Baxter and T. Reda, *Phys. Rev. B: Condens. Matter Mater. Phys.*, 2002, **66**, 075417.
24 J. Jasieniak, M. Califano and S. E. Watkins, *ACS Nano*, 2011, **5**, 5888.
25 D. Shahar and Z. Ovadyahu, *Phys. Rev. Lett.*, 1990, **64**, 2293.